Coherent Fourier scatterometry for detection of nanometer-sized particles on a planar substrate surface

S. Roy,* A. C. Assafrão, S. F. Pereira, and H. P. Urbach

Optics Research Group, Department of Imaging Physics, Delft University of Technology, Van der Waalsweg 8, 2628 CH Delft, Netherlands

*S.Roy@tudelft.nl

Abstract: Inspection tools for nano-particle contamination on a planar substrate surface is a critical problem in micro-electronics. The present solutions are either expensive and slow or inexpensive and fast but have low sensitivity because of limitations due to diffraction. Most of them are also substrate specific. In this article we report how Coherent Fourier Scatterometry is used for detection of particles smaller than $\lambda/4$. Merits of the technique, especially, the procedures to improve SNR, its flexibility and its robustness on rough surfaces are discussed with simulated and experimental results.

OCIS codes: (120.4630) Optical inspection; (070.0070) Fourier optics and signal processing; (120.5820) Scattering measurements; (170.5810) Scanning microscopy.

References and links

1. O. El Gawhary, N. Kumar, S. F. Pereira, W. M. J. Coene, and H. P. Urbach, "Performance analysis of coherent optical scatterometry," Appl. Phys. B **105**(4), 775–781 (2006).
2. V. F. Paz, S. Peterhnsel, K. Frenner, and W. Osten, "Solving the inverse grating problem by white light interference Fourier scatterometry," Light Sci. Appl. **1**(36), 1–7 (2012).
3. A. J. M. den Boef , A. J. Bleeker, Y. J. L. M. van Dommenlen, M. Dusa, A. G. M. Kiers, P. F. Luehrmann, H. P. M. Pellemans, M. van der Schaar , C. D. Grouwstra, and M. G. G. M. van Kraaij, "Method and apparatus for angular-resolved spectroscopic lithography characterisation," European Patent EP1628164, (2006).
4. J. Berger, *Detection of Particles on Clean Surfaces* (Springer, 1989).
5. U. Okoroanyanwu, J. Heumann, X. Zhu, C. H. Clifford, F. Jiang, P. Mangat, R. Ghaskadavi, E. Mohn, R. Moses, O. Wood, H. Rolff, T. Schedel, R. Cantrell, P. Nesladek, N. LiCausi, X. Cai, W. Taylor, J. Schefske, M. Bender, and N. Schmidt, "Towards the optical inspection sensitivity optimization of EUV masks and EUVL-exposed wafers," Proc. SPIE. **8352**, 83520V (2012).
6. V. Bakshi, ed., E*UV Lithography* (SPIE Press, 2009), pp.360–362.
7. N. Engheta, "Circuits with light at nanoscales: optical nanocircuits inspired by metamaterials," Science **317**(5845), 1698–1702 (2007).
8. H. Oerley, "Metrology systems for quality and process control of coatings on glass and plastic films," in Proceedings of *Technical Session 4, 9th International Conference on Coatings on Glass and Plastics 2012*, Breda, Netherlands.
9. J. F. Aguilar, and E. R. Méndez, "On the limitations of the confocal scanning optical microscope as a profilometer," J. Mod. Opt. **42**(9), 1785–1794 (1995).
10. H. R. Huff, R. K. Goodall, E. Williams, K. Woo, B. Y. H. Liu, T. Warner, D. Hirleman, K. Gildersleeve, W. M. Bullis, B. W. Scheer, and J. Stover, "Measurement of silicon particles by laser surface scanning and angle-resolved light scattering," J. Electrochem. Soc. **144**(1), 243–250 (1997).
11. A. Okamoto, H. Kuniyasu, and H. Takeshi, "Detection of 3040-nm particles on bulk-silicon and SOI wafers using deep UV laser scattering," IEEE Trans. Semicond. Manuf. **19**(4), 372–380 (2006).
12. T. A. Germer, "Multidetector hemispherical polarized optical scattering instrument," Proc SPIE **3784**, 304–313 (1999).

#205252 - $15.00 USD Received 3 Mar 2014; revised 19 Apr 2014; accepted 24 Apr 2014; published 27 May 2014

13. A. Chen, V. Huang, S. Chen, C. J. Tsai, K. Wu, H. Zhang, K. Sun, J. Saito, H. Chen, D. Hu, M. Li, W. Shen, and U. Mahajan, "Advanced inspection methodologies for detection and classification of killer substrate defects," Proc. SPIE **7140**, 71400W (2008).
14. T. A. Germer, "Angular dependence and polarization of out-of-plane optical scattering from particulate contamination, subsurface defects, and surface microroughness," Appl. Opt. *36*, 8798–8805 (1997).
15. J. C. Stover, V. I. Ivakhnenko, and Y. Eremin, "The use of light scatter signals to identify particle material" Proc. SPIE **4449**, 131–139 (2001).
16. N. Kumar, O. El Gawhary, S. Roy, V. G. Kutchoukov, S. F. Pereira, W. Coene, and H. P. Urbach, "Coherent Fourier scatterometry: tool for improved sensitivity in semiconductor metrology," Proc. SPIE **8324**, 83240Q (2012);
17. A. C. Assafrão, A. J. H. Wachters, S. F. Pereira, and H. P. Urbach, "Near-field self-induced hollow spot through localized heating of polycarbonate/ZnS stack layer," Appl. Opt. **51**(31), 7684–7689 (2012).
18. B. E. Roberds and S. N. Farrens, "An atomic force microscopy study on the roughness of silicon wafers correlated with direct wafer bonding," J. Electrochem. Soc. **143**(7), 2365–2371 (1996).
19. C. Teichert, J. F. MacKay, D. E. Savage, and M. G. Lagally,"Comparison of surface roughness of polished silicon wafers measured by light scattering topography, soft-x-ray scattering, and atomic-force microscopy," Appl. Phys. Lett. **66**(18), 2346–2348 (1995).
20. S. Harkema, S. Mennema, M. Barink, H Rooms, J. S. Wilson, T. van Moland, and D. Bollen "Large area ITO-free flexible white OLEDs with orgacon PEDOT:PSS and printed metal shunting lines," Proc. SPIE **7415**, 74150T (2009).
21. G. Videen, "Light scattering from a sphere on or near a surface," J. Opt. Soc. Am. A **8**(3), 483–489 (1991).
22. B. R. Johnson, "Calculation of light scattering from a spherical particle on a surface by the multipole expansion method," J. Opt. Soc. Am. A **13**(2), 326–337 (1996).
23. R. Schmehl, B. M. Nebeker, and E. D. Hirleman, "Discrete-dipole approximation for scattering by features on surfaces by means of a two-dimensional fast Fourier transform technique," J. Opt. Soc. Am. A **14**(11), 3026–3036 (1997).
24. X. Wei, A. J. H. Wachters, and H. P. Urbach, "Finite-element model for three-dimensional optical scattering problems," J. Opt. Soc. Am. A **24**(3), 866–881 (2007).
25. P. Blake, E. W. Hill, A. H. Castro Neto, K. S. Novoselov, D. Jiang, R. Yang, T. J. Booth, and A. K. Geim, "Making graphene visible," Appl. Phys. Lett. **91**(6), 063124 (2007).
26. O. G. Rodríguez-Herrera, D. Lara, K. Y. Bliokh, E. A. Ostrovskaya, and C. Dainty, "Optical nanoprobing via spin-orbit interaction of light," Phys. Rev. Lett. **104**(25), 253601 (2010).
27. T. Herffurth, S. Schrder, M. Trost, A. Duparr, and A. Tnnermann, "Comprehensive nanostructure and defect analysis using a simple 3D light-scatter sensor," Appl. Opt. **52**(14), 3279–3287 (2013).
28. C. Amra, "Light scattering from multilayer optics. II. Application to experiment," J. Opt. Soc. Am. A **11**, 211–226 (1994).
29. Y. A. Eremin, J. C. Stover, and N. V. Orlov "Modeling scatter from silicon wafers features based on discrete sources method," Opt. Eng. **38**, 1296–1304 (1999).

1. Introduction

Coherent Fourier Scatterometry (CFS) is a scanning based scatterometry technique which has been used in the field of metrology of periodic structures [1, 2]. The main advantage in using CFS compared to conventional Incoherent Fourier Scatterometry [3] is the smaller spot size and the presence of the implicit phase information in the far field intensity patterns, possible only under coherent illumination. Although reconstruction of periodic structures was the primary objective of CFS, it is an interesting question to evaluate the performance of CFS on non-periodic structures, in particular, isolated elements.

The problem of detecting isolated nano-particles [4] or small damages on a surface is an important requirement arising in many practical situations. One example is semiconductor manufacturing process, where silicon wafers need to be cleaned thoroughly to eliminate the 'killer particles' prior to further processing. With the advent of substrates like organic electroluminescent materials, having completely different surface topology than silicon, or EUV lithography with more stringent cleaning requirement [5, 6], this problem is getting more diversified, critical and challenging now-a-days. Besides detection, locating the detected particles and classifying them according to their sizes without carrying out any additional measurement is also a desirable additional information required in many practical situations other than those mentioned

#205252 - $15.00 USD Received 3 Mar 2014; revised 19 Apr 2014; accepted 24 Apr 2014; published 27 May 2014

above, for example, engineering of optical nano-circuits [7].

A sizable portion of the optical solutions for this inspection problem employs imaging techniques [8] or confocal imaging technology [9], due to the simplicity and robustness of an imaging-based process. However, the limitation for these methods is a very low signal to noise ratio (SNR), especially for particles close to diffraction limit. Conversely, scattering based techniques may be favored for detecting particle in this regime [10]. In general, in the CFS technique, imaging is avoided and the far field intensity pattern is captured over a large detector area. Therefore, one could, theoretically, extract information from selected parts of the pupil and/or use polarization effects to enhance the SNR. While possessing most benefits of an imaging-based technique, CFS is simpler to configure and more versatile than other scattering based techniques, as for example the one described in [11]. The basic setup for scattering based optical inspection tools are shown in Fig. 1(a). The laser beam is focused onto the sample from a high angle of incidence, and the reflected signal together with scattered signal is detected by multiple detectors [12]. The drawbacks include a complex experimental arrangement, slower and expensive operation and small room for further modification. The state of the art commercial scanners, that employs this technique in a dual-laser variation (for example KLA-Tencor Candela series), has reached sensitivities of about 60-80 nm (with dual wavelength illumination of 405 and 350 nm), whereas more specialized ones, which uses shorter wavelengths, are able to detect about 40 nm particles [13]. One more benefit of scattering based methods, including CFS (Fig. 1(b)), is that they employ a focused spot of a very small area so that the local departure from flatness of the substrate does not play a large role. Furthermore, the complexity of the experimental arrangement is greatly reduced by employing one single lens to focus and collect the reflected light. High angles of incidence are achieved by using objective with high numerical apertures.

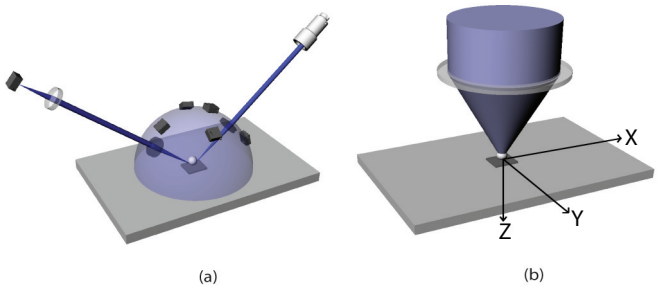

Fig. 1. The standard scattering based surface scanning techniques employing a focused laser beam at large angle of incidence is shown in (a). Generally, in these 'classical' goniometric scatterometers, the specularly reflected and scattered intensities are respectively measured with a fixed and a movable detector. Many detector positions are necessary if it is required to measure the scattered intensity as a function of angle, which leads to slower operation. More complex systems with more measurements can distinguish between scattering from a contamination or surface roughness [14] or can determine the contaminating material [15]. The illumination of CFS along with the co-ordinate system to be used in the article are shown in (b). CFS requires a single shot measurement other than procedures employing angular laser-scanning techniques. The optical axis (z) is positive downwards with the origin at the geometric focus of the objective.

In this paper we present the performance of CFS for detecting isolated elements as small as 100 nm. Our experimental setup utilizes a coherent source of 405 nm with an objective

#205252 - $15.00 USD Received 3 Mar 2014; revised 19 Apr 2014; accepted 24 Apr 2014; published 27 May 2014

of numerical aperture (NA) of 0.9, which implies that the samples contain particles smaller than conventional diffraction limit associated with the confocal microscopy, namely $\lambda/4NA$. We also show to predict the approximate location and size of the nano-particle, without making additional measurements. The versatility and possible ways to increase sensitivity are discussed in detail.

The remainder of this paper is organized as follows: in the next section we briefly describe the experimental setup and the samples examined, including the procedure for preparation of each of them. In section 3 we first consider the electromagnetic problem of interaction of a spherical particle on a flat isotropic substrate illuminated by a focused field of coherent illumination and solve the problem numerically. This helps us to do a feasibility study to check whether a CFS system with given parameters is able to detect contaminating particles of a given size, and if that is the case, to determine the sensitivity. We proceed by showing the experimental results. A direct comparison between theory and experiment is provided. Finally we discuss methods to increase the SNR for small particles. The conclusions of this work are given in Section 4.

2. Experimental setup and preparation of the samples

2.1. Setup

In Fig. 2, the experimental setup of CFS is shown [16, 17]. A commercial scanning near-field optical microscope (Witec Alpha 300S), largely modified to operate simultaneously as a CFS and conventional microscope. The advantage of having a conventional microscope is to have the possibility of visually confirming whether the signal generated by CFS is coming from the contaminating particles and not from something else. Naturally, it works for particles larger than 200 nm for which it is possible to directly image them. Moreover, the conventional microscope helps to set up the CFS by imaging the sample plane, which, if the CFS is set up correctly, should contain the focused spot. This plane is imaged in CAMERA1. The conventional microscope part uses a white light source (COL2) whereas the CFS part uses a diode laser operating at 405 nm. The laser beam is coupled into a single mode fiber and redirected to the main part of the setup through the collimator COL1. The light from the COL1 is made linearly polarized (POL1) before it passes through the beam-splitter (BS1) and focused by the objective (OBJ). Other elements can be easily inserted along the light path in order to obtain any desired input polarization other than linear. The objective position in the axial z-direction can be adjusted by a stepper motor to aid focusing, up to a precision of 50 nm. The sample is placed on the scanning table (STAGE) driven by a piezo-transducer which can move the sample in raster mode to perform scanning of the area of interest. The reflected field from the sample is captured by OBJ, and the output polarization is set by polarizer (POL2). A telescopic arrangement is formed by LENS2 and LENS3 to fit the reflected beam into the camera aperture (CAMERA2). The set-up is kept in a temperature controlled clean room.

2.2. Samples

We will consider two types of samples here. The first type consists of polystyrene latex (PSL) nano-spheres of diameters 400 nm, 200 nm and 100 nm deposited on a silicon wafer with rms roughness less than 3 nm (this agrees with standard silicon wafer roughness measurement, for example [18, 19]) in the shape of a disc of diameter 2.54 mm, with densities of approximately 1300/sq. mm, 4100/sq. mm and 26000/sq. mm, respectively. To deposit the particles, mono-disperse PSL colloidal suspension (stabilized by ultra-sonic treatment and shaking) was dispersed on the substrate, cleaned with UV-ozone treatment, by spin-coating. The second type of sample is an organic light emitting diode (OLED) deposited on a square glass substrate of size 25 mm. In those samples, firstly poly-3,4-ethylenedioxythiophene (PEDOT): poly-styrenesulfonate (PSS) was spin-coated on top of ITO on a glass substrate to fabricate

#205252 - $15.00 USD Received 3 Mar 2014; revised 19 Apr 2014; accepted 24 Apr 2014; published 27 May 2014

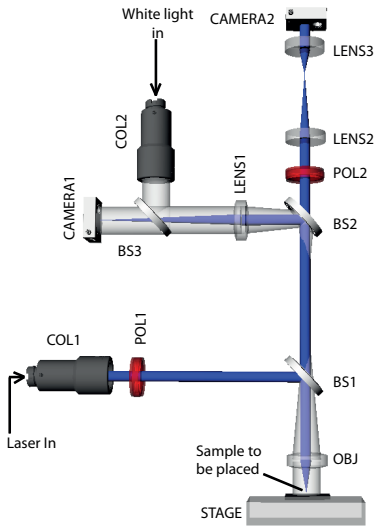

Fig. 2. The experimental setup of CFS. Outline is described in detail in the text. The measurements are performed in reflection.

the anode. The light-emitting polymer (LEP) was spin-coated from toluene on top of the PEDOT:PSS. At the last stage a Ba-Al cathode was fabricated by thermally evaporating 5 nm Ba and 100 nm Al through a shadow mask ([20]). An atomic force microscope (AFM) scan of the sample surface is shown in Fig. 3, for different area. The surface is damaged at several locations in form of pinholes. The samples with nano-spheres are suitable for determination of the limit of sensitivity of CFS for isolated particles, while the OLED samples are used to verify whether CFS can be used to distinguish the difference between defects of different sizes on a sample with non-negligible surface roughness.

3. Results of implementation

3.1. The numerical model

The electromagnetic problem of the interaction of a spherical particle on a plane surface with an incident plane wave is interesting from a theoretical point of view and has been studied by many authors in detail [21, 22]. A detailed study on numerical methods targeted especially for this problem [23], albeit interesting, is beyond the scope of this paper. For our simulations we have used rigorous three dimensional finite elements method (3D-FEM) [24]. To mimic the experimental conditions, we consider an objective lens with numerical aperture NA=0.9 focuses a plane wave of wavelength of 405nm. This focused field interacts a PSL particle (refractive index = 1.58) placed on a silicon wafer substrate of index $5.42+0.33j$ in air [25]. The structure of the simulation model is shown in Fig. 4. The permittivity function is summarized by

$$\begin{aligned}\varepsilon(x,y,z) &= 1 \text{ if } z \le 0 \text{ and } x^2+y^2+(z-D/2)^2 > D/2 \\ &= (1.58)^2 \text{ if } z \le 0 \text{ and } x^2+y^2+(z-D/2)^2 \le D/2 \\ &= (5.42+0.33j)^2 \text{ if } z > 0 \end{aligned} \quad (1)$$

where D is the diameter of the particle.

#205252 - $15.00 USD Received 3 Mar 2014; revised 19 Apr 2014; accepted 24 Apr 2014; published 27 May 2014

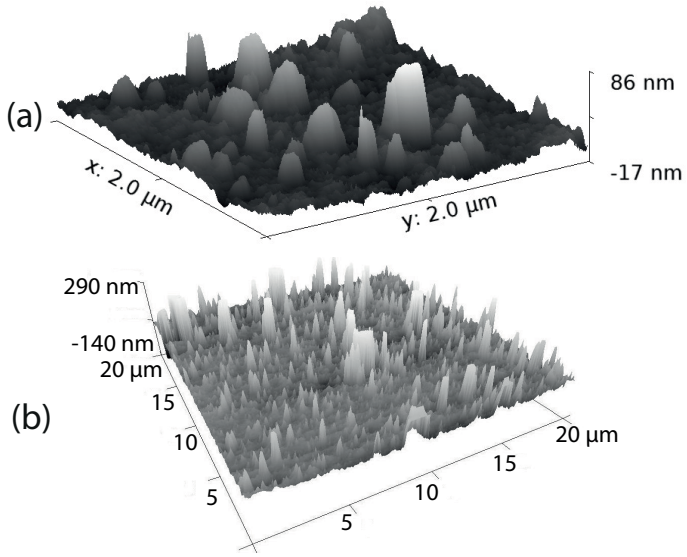

Fig. 3. The AFM scan of the bare OLED sample. Water ingress into the pinholes in the cathode caused by the presence of particles, leads to an oxidation of the Al at the cathode-LEP interface. At these locations the electron injection is blocked, resulting in a local absence of emission, visible as a so-called black spot, or pinhole (see also Fig. 8(a)). (a) For an area of roughly the spot size, the rms roughness is about 9.5 nm. Due to numerous defects, the rms roughness rapidly increases for larger areas. In (b) it is about 30 nm for an area of 20 μm square. This typically large roughness is probably due to degradation of cathode, where due to gas formation underneath the cathode when water reacts with aluminum, roughness increases.

The easiest case to experimentally realize is when linear polarizers are used in the incident and scattered field path (POL1 and POL2 in Fig. 2). It is possible to select specific combination of POL1 and POL2 to obtain sufficient information to obtain the polarization ellipse for each pixel in CAMERA2. However, measuring all these polarization schemes, which should improve the sensitivity, is more complex to implement and can be investigated if the linear polarization schemes would not generate sufficient sensitivity [26]. To obtain the detection signal, the normalized power through the pupil is calculated. We define the normalized power as the power in the pupil for each frame obtained during scanning divided by the power in the pupil of a reference frame (the frame in which the particle is sufficiently far from the focused spot to have detectable influence in the scattered field) of a specific polarization scheme. This normalization procedure helps us plot results for different samples in the same scale, and also to decrease the effects due to imperfection in optical elements. After the normalization, values that differ from unity indicate the presence of the particle. Mathematically, it can be defined as,

$$\text{Normalized power} = \frac{\sum_{p=1}^{M}\sum_{q=1}^{M} I_{p,q}}{\sum_{p=1}^{M}\sum_{q=1}^{M} I_{p,q}^{ref}} \tag{2}$$

where, $I_{p,q}$ is the scattered intensity at the (p,q)th pixel and $I_{p,q}^{ref}$ is the same for the reference frame. M is the total number of pixels in one side of the square pupil frame and is equal to 100

#205252 - $15.00 USD Received 3 Mar 2014; revised 19 Apr 2014; accepted 24 Apr 2014; published 27 May 2014

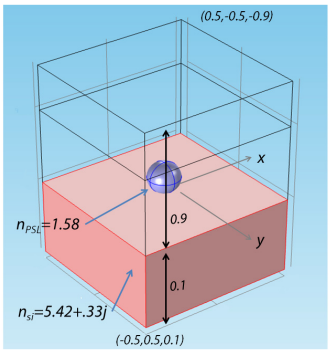

Fig. 4. The numerical modeling of the problem. The simulation scheme is a cube of 1 μm enclosed by a perfect matched layer boundary. All numbers are in μm. Co-ordinate system is in accordance with Fig. 1(b). The co-ordinates of two diagonally opposite point are given. The air-silicon interface, containing the geometric focus, lies at $z = 0$ where the z axis (not shown)is the instrument's optical axis, with positive z downwards. The incident wave is a beam focused at origin with the numerical aperture of 0.9, divided in to 10^4 incident angles. The mesh size was chosen in such way that the first zero in the focused electric field components fit completely inside the computational domain, for the numerical aperture considered. Also, adaptive meshing was employed to assign higher number of points in the central region of the computation domain.

for the simulation and 572 for CAMERA2. In the way normalized power is defined, it will be finite even if the power in some pixels of reference frame is very small. The normalized power is generally smaller than unity (as the light is scattered out) for linear polarized (LP) incident light with the second polarizer parallel to it at the detection path (hereafter called parallel LP-LP, polarized along x) and larger than unity for crossed LP-LP (second polarizer POL2 orthogonal to the first polarizer POL1). The primary feasibility study, for parallel LP-LP, is shown in Fig. 5 along with the experimental results. The sample with PSL particles on silicon wafer was used. From these results, detection seems feasible, though with a low SNR for particle size up to 100 nm.

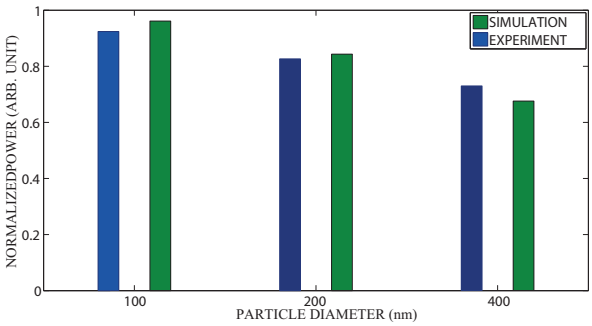

Fig. 5. The simulated and measured normalized power for particles with varying diameters. The particles are inside the focused spot. Any deviation from unity indicates that the particle can be detected.

#205252 - $15.00 USD Received 3 Mar 2014; revised 19 Apr 2014; accepted 24 Apr 2014; published 27 May 2014

3.2. *Experimental results*

As mentioned before, we consider primarily the parallel LP-LP case, with the particle positioned underneath the center of the focused spot. The simulated far field with normalized intensity (with reference) is shown in Fig. 6(a). The corresponding experimental result for reference and with the presence of a particle is shown in in the Fig. 6(b) and Fig. 6(c), respectively. The experiment data normalized with the reference intensity pattern, pixel by pixel, is shown in the Fig. 6(d). Similar intensity distribution in the pupil can be seen between 6(a) and 6(d). Even better agreement is obtained when the central bright spot is eliminated by normalization (see Fig. 6(c)). The central bright spot comes from the internal reflection between the optical components. There is a small asymmetry in the experimental data, likely caused by a small misalignment between the center of the spot and the center of the sphere, which is assumed to be zero in simulation. Nonetheless, both simulation and experiment are consistent with each other, validating thus the numerical model for describing the phenomena.

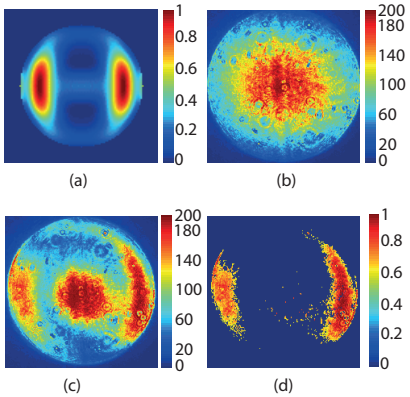

Fig. 6. Comparison of simulated and measured far field distribution of a single 100nm particle under the focused spot, using the parallel LP-LP mode. The transverse axis used in the far field is parallel to the one defined in Fig. 1(b). (a) The simulation result is shown. In (b) Experimental data for reference and (c) experimental data in presence of a particle is shown after binning. (d) is generated by pixel by pixel normalizing (c) by reference (b), to reduce the central bright spot. The presence of large power along the edges of the pupil in the direction of polarization is the main indication for presence of particle. The symmetry indicates the center of the particle to be almost on optical axis.

We now consider a raster scanning of a given sample. The normalized power is plotted as function of the scan distance in one direction. The starting position for each scan line is take as the reference intensity pattern for that line. The scheme of the raster scanning for 100 nm particle is shown in Fig. 7(a). Forward scans were used to capture the data frames. The reinitialization to the next line consists of a backward movement to the initial position followed by a downward cruise to the next line. During this time, no frames are captured. In Fig. 7(b) the detected signal of each particle is shown. The abscissa shows the shift from the initial scan position, in μm. Starting from a position far from the sphere (normalized power equal to unity), one can immediately notice a dip in the signal due to the presence of the particle due to scattering.

The SNR is large for the 400nm particles and diminishes as the size of the illuminated object diminishes. At 100nm, for the best scan line at $y = 100nm$, the peak is less than 5%, but still distinguishable from the background noise. This results ultimately indicate that a simple integration method can result in the detection of particles as small as 100nm, a function that can be readily performed by a single photo-detector, rather than a CCD camera. We will now proceed

#205252 - $15.00 USD Received 3 Mar 2014; revised 19 Apr 2014; accepted 24 Apr 2014; published 27 May 2014

by showing methods to enhance the SNR of the detected signal of 100nm particles.

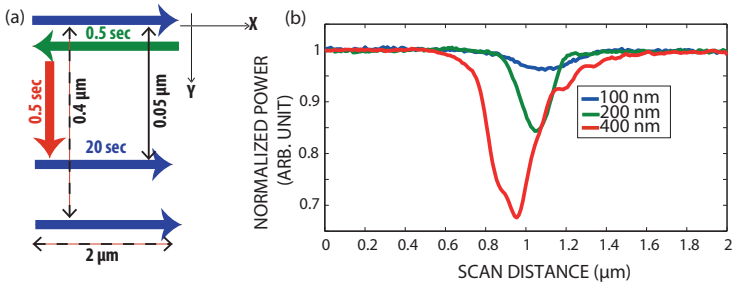

Fig. 7. Detection of particle contamination with CFS. (a) The scheme of the raster scanning method employed. Each scan line (blue) of 2 μm takes 20 seconds and generates 200 frames. Reinitialization to next line takes 1 sec, with backward movement (green) and a downward cruise (red), generating 10 frames that are not captured by the camera. The total scan area, for this case, is 2 μm by 0.4 μm. The scheme stays identical for larger particles but the shift between two lines is increased, resulting in larger scan area. (b) Normalized power against shift from initial scan position (scan distance, in μm) for particles of 400 nm (red), 200 nm (green) and 100 nm (blue). Signals with large SNR are generated by the larger particles. The bottom of the dip coincides with the center of the nano-sphere. Those frames were considered to generate the experimental data points in Fig. 5.

3.3. Enhancement of the SNR for 100 nm particle

3.3.1. Blockage of inner part of the pupil

Although all particles considered have been detected by the CFS, a low SNR for the 100nm was obtained. Because the scattering varies by the sixth power of the diameter [10], the scattering from 100 nm particle is about 0.02% of that from a 400 nm particle. Therefore, it is desirable to have a method to enhance the readout signal of small particles. Luckily, CFS offers an elegant solution to this problem. Since one would expect that the field at large angles will be more influenced by the particle than field at the smaller angles, the SNR of the readout signal can be enhanced if only the outer parts of the far-field distribution are integrated. Furthermore, spurious reflections from the optical elements that occur mostly near the central part of the pupil would be eliminated, increasing thus the SNR. We will now apply this concept to experimentally evaluate whether the SNR can indeed be improved.

In Fig. 8(a), the normalized power for the best scan line is plotted as function of the scan distance for different blockages of the inner part of the pupil. The results indicate an optimal improvement in the signal for the case of blocking NA=0.5 for this special case. This result is supported from the simulation results, as shown in Fig. 8(b), where the trend predicted by simulation is approximately followed by the practical data. Another interesting result arises from the crossed LP-LP case. If there is no particle underneath the focused spot, a darker background is seen in the detector. However, the total power through the pupil was still finite. Whenever the particle is illuminated, the depolarized field introduced by the particle becomes visible in the far-field as more light is scattered in the pupil. As a result, a larger peak-to-peak readout signal is obtained, as seen in Fig. 8(c) for the best scan line. The simulated and experimental results are compared in Fig. 8(d).

#205252 - $15.00 USD Received 3 Mar 2014; revised 19 Apr 2014; accepted 24 Apr 2014; published 27 May 2014

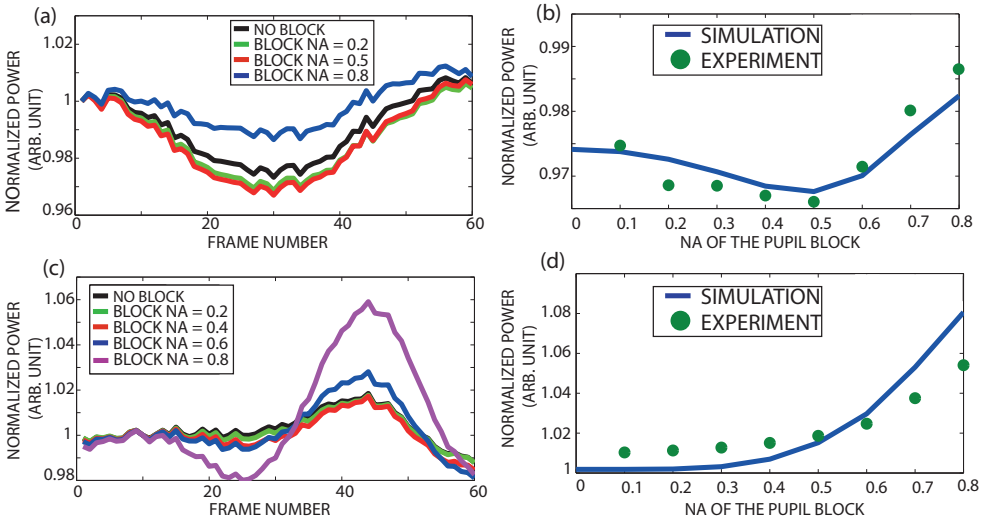

Fig. 8. Detection signal of 100nm PSL sphere with *NA* till which the pupil is blocked from the center.(a) The improvement of the signal for 100 nm particle with different amount of blocking in the pupil is shown for parallel LP-LP scheme. (b) The comparison of the theoretical and practical data for parallel LP-LP. The optimum amount of blocking is found to about $NA = 0.5$ for this case. (c) shows the results for crossed LP-LP scheme. The blocking improves the SNR monotonically for this case. (d) comparison between simulation and experiment for case (c).

3.3.2. The asymmetry in the far field

Up to now we have integrated the output signal either over the entire pupil or in the outer parts of it. A third type of integration would consist of using quadrant detection. The motivation for quadrant detection comes from the fact that any loss of symmetry in the far field [26] caused by the particle could be immediately observed in the output signal. Therefore, by dividing the pupil into quadrants of equal area and calculating the asymmetry of power distribution between them, thereby obtaining an approximate quadrant detector (QD), there is a possibility of achieving better SNR. Experimentally this would mean to replace CAMERA2 with a quadrant detector.

We shall consider this detection scheme in what follows. In top left of Fig. 9, the schematics of the QD is shown. The results of this analysis for a 100 nm particle with parallel LP-LP scheme, normalized by the first frame of the scan line, is shown in Fig. 9(a) after applying a pupil blocking of $NA = 0.5$ from center. The blue line shows the detection based on normalized power, similar to Fig. 9(a), while the green lines show the signal obtained from approximate QD. The dashed green line, designated $QDL - R$, shows the difference in power between left and right part of the approximate QD, while the dotted green line ($QDT - B$) shows the same for top and bottom quadrant. The solid green line is the average of the maximum and minimum signal from $QDL - R$, can be considered as zero line (ZL). Mathematically, the QD signals are evaluated as

$$QDL - R = \frac{\sum_{p=1}^{M/2}\sum_{q=1}^{M} I_{p,q} - \sum_{p=M/2+1}^{M}\sum_{q=1}^{M} I_{p,q}}{max\left|\sum_{p=1}^{M/2}\sum_{q=1}^{M} I_{p,q} - \sum_{p=M/2+1}^{M}\sum_{q=1}^{M} I_{p,q}\right|}. \quad (3)$$

#205252 - $15.00 USD Received 3 Mar 2014; revised 19 Apr 2014; accepted 24 Apr 2014; published 27 May 2014

Then $QDL - R$ was set to zero for the first frame (the reference), and the maximization is calculated over all frames (scan positions). Similarly $QDT - B$ was evaluated.

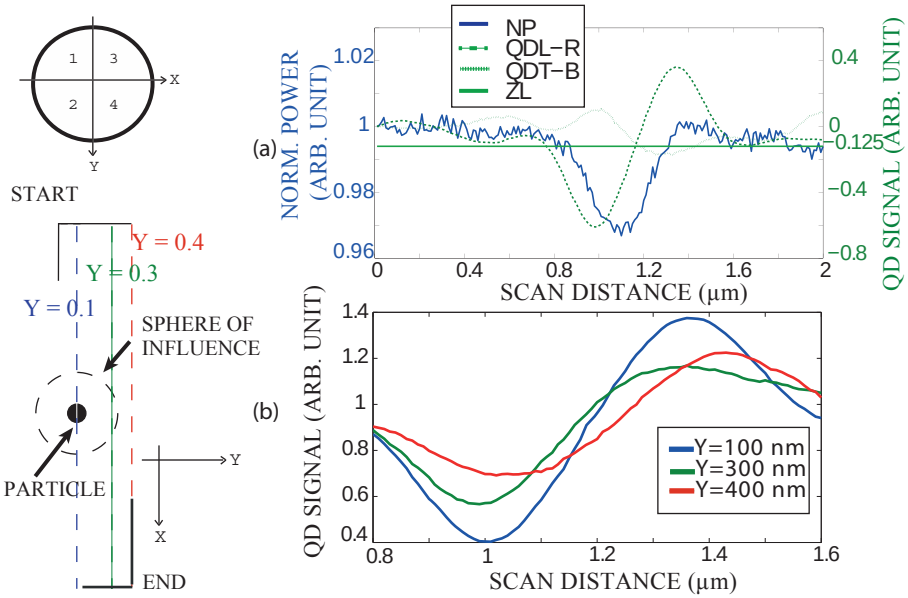

Fig. 9. Application of QD approximation on the data obtained for 100 nm particle. (a) For the best scan line at $y = 100nm$, the normalized power analysis (similar to Fig. 7) is shown in blue, while different cases of quadrant detector approximation are shown in green. The schematic QD is shown in top left. The scale for QD signal is 20 times the signal from normalized power analysis. The fact that QDL-R is more sensitive than QDT-B indicates that when the scanning was done, the particle was approached by moving from left to right. (b) The decrease of SNR as the spot moves away from the particle in Y-direction. The blue line is the scan at $y = 100nm$, green at $y = 300nm$ and red at $y = 400nm$, relative to scan origin. It may be seen that the particle can be detected at a distance of about 200 nm away on each side of the particle. Assuming the scan line with the maximum SNR is closest to the particle center, approximate location of the particle in the scan area, along with the area over which it can be detected (dashed line), is shown on the bottom left. In this figure, the axis orientation is interchanged for drawing convenience. All co-ordinates in μm. More precise results can be obtained with a finer scanning and a better reference.

There are few things to note here. Firstly, improvement of SNR by almost twice of an order is observed (the scale for QD signal is 20 times as large as the scale of normalized power), especially in QDR-L, supporting the practicality of using asymmetry in field distribution for particle detection. Secondly, the fact that the particle has been approached more from left to right than from top to bottom, as evident from the signal amplitude gives a relative indication of the direction of the particle from the initial scanning position. Thirdly, the approximate center of the particle can be found as the point of interaction of the ZL with QDL-R. ZL corresponds to the case when the field has very small asymmetry, which happens when the spot is far from the particle or when the particle is best aligned with the z-axis or the optical axis. If the illumination was ideally planar and the reference frame was captured when the spot is infinitely far away from the particle ZL should pass through zero. In practice small field asymmetry is always present in the reference which sifts ZL slightly away from zero. Calculation of the approximate position of the particle can be done from the intersection of this 'practical zero line' ZL and

#205252 - $15.00 USD Received 3 Mar 2014; revised 19 Apr 2014; accepted 24 Apr 2014; published 27 May 2014

the signal. Moreover, a scan through the center of the particle QDT-B should also pass through this point and this should also correspond to the minimum of the normalized power. These results are seen in Fig. 9(a), for the best scan line at $y = 100nm$, where the maximum SNR was achieved (refer to Fig. 7(a)). In Fig. 9(b), the fall of SNR is shown as the scanning spot moves further away from the center of the particle. However, detectable signal still exists for a scan at $y = 300nm$, implying an area of diameter 200nm influenced by the presence of the particle. In the figure on bottom left, the position of the particle, its 'sphere of influence', and the scan lines are shown schematically in the scan area.

3.4. Samples with large roughness and size classification

In order to verify whether the CFS system can differentiate between particle sizes, and also, whether it can work on a surface with substantial roughness, the OLED sample is tested. Note that with the previous example, a direct comparison between sizes of the particles cannot be confirmed as the particles of different sizes were deposited on different samples, and it is quite probable that the exact experimental parameters (like focusing, reflection) will change slightly as one sample is removed and another is reinserted. Thus a better comparison can be done only if the same sample contains defects of different sizes. For this purpose, the OLED sample which contains defects with the shape of pinholes of various sizes on it is used. Figure 10(a) is an image of the surface of the OLED, where two pinholes in close vicinity but of different sizes are marked out. In Fig. 10(b) we observe how this difference in size is visible in readout signal. From this, we can conclude that if a CFS system is calibrated for defects of known sizes, it can then give an approximate value of the particle size while detecting the particle, without making any additional measurement. Moreover, CFS is able to detect defects in an Al layer having substantial surface roughness.

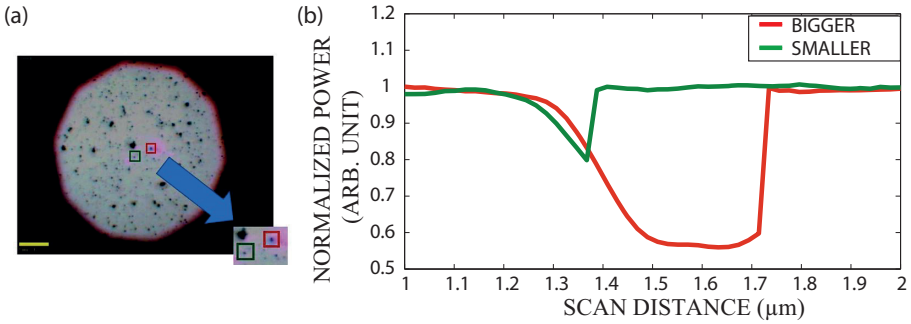

Fig. 10. Difference of defect sizes as detected by CFS. In (a) the image of the sample size using the white light source is shown with two pinhole defects of different sizes. The bigger boxed in red, smaller boxed in green. The sizes of the smaller one is approximately 200-220 nm, while the bigger one is about 400-420 nm. The signal after they were scanned is shown in (b), using the same scanning parameters. The difference in sizes is evident from the scanning distances for which the normalized power is smaller than the reference.

4. Conclusion

In this paper we have discussed how Coherent Fourier Scatterometry (CFS) can be applied in the problem of detection of isolated particles and also shown how it can be used to detect particles down to size of diameter 100 nm on a silicon wafer surface. We mentioned how this method can distinguish between various defect sizes on an OLED sample. We showed how enhanced SNR can be achieved by employing partial blocking of the aperture and how this can

#205252 - $15.00 USD Received 3 Mar 2014; revised 19 Apr 2014; accepted 24 Apr 2014; published 27 May 2014

be predicted from the numerical model. Presence of the particle slightly away from the axis of the instrument creates far-field power distribution which is asymmetric, we have shown that by using this loss of symmetry can be used to detect the scatterer with an enhanced SNR. Both of these techniques of SNR enhancement can be applied together to facilitate the detection. The experiments were performed in the most simple configuration possible which implies that higher sensitivity, if required, can be achieved by using more complex polarization control, structured illumination or with some data processing of different kind, without reducing the illumination wavelength. It may be noted that the simplicity of the method lies not only in its practical implementation but also in the analysis of the data it produces, since simple measurement like change in the amount of power through the pupil can be used for successful particle detection compared to some recent methods introduced in this field [27]. The advantage here is a compact design, employing single source-single detector configuration with normal incidence which is easily upgradable to parallel implementation of multiple scanners. The penalty to ensure compact and faster operation of CFS than classical single source-multiple detector type goniometric scanners is somewhat limited resolution and the inability to classify defects from contamination or roughness. This information to differentiate, present in the scattered field [28, 29], may be possible to be retrieved in CFS if the complete intensity distribution in the far field is analyzed. However, this requires further research.

Acknowledgments

S. Roy would like to acknowledge the help of Nishant Kumar of Delft University of Technology for providing the AFM measurements, Christiaan Hollemans and Harmen Rooms of TNO for providing the samples and Hans Oerley and Simone Dafinger of Dr. Schenk GmbH for their inputs in this work. The authors acknowledge European Union's Seventh Framework Program (FP7/2007-2013) under grant agreement no. 281027 for funding this research.